Smart Structures and Systems, *Vol. 28, No. 6 (2021) 827-838*
https://doi.org/10.12989/sss.2021.28.6.827

Indirect displacement monitoring of high-speed railway box girders consider bending and torsion coupling effects

Xin Wang [1b], Zhonglong Li [1a], Yi Zhuo [2a], Hao Di [2], Jianfeng Wei [2], Yuchen Li [1] and Shunlong Li*[1]

[1] *School of Transportation Science and Engineering, Harbin Institute of Technology, 73 Huanghe Road, 150090 Harbin, China*
[2] *China Railway Design Corporation, 300142 Tianjin, China*

(*Received June 1, 2021, Revised September 15, 2021, Accepted September 17, 2021*)

Abstract. The dynamic displacement is considered to be an important indicator of structural safety, and becomes an indispensable part of Structural Health Monitoring (SHM) system for high-speed railway bridges. This paper proposes an indirect strain based dynamic displacement reconstruction methodology for high-speed railway box girders. For the typical box girders under eccentric train load, the plane section assumption and elementary beam theory is no longer applicable due to the bend-torsion coupling effects. The monitored strain was decoupled into bend and torsion induced strain, pre-trained multi-output support vector regression (M-SVR) model was employed for such decoupling process considering the sensor layout cost and reconstruction accuracy. The decoupled strained based displacement could be reconstructed respectively using box girder plate element analysis and mode superposition principle. For the transformation modal matrix has a significant impact on the reconstructed displacement accuracy, the modal order would be optimized using particle swarm algorithm (PSO), aiming to minimize the ill conditioned degree of transformation modal matrix and the displacement reconstruction error. Numerical simulation and dynamic load testing results show that the reconstructed displacement was in good agreement with the simulated or measured results, which verifies the validity and accuracy of the algorithm proposed in this paper.

Keywords: bend-torsion coupling effects; displacement reconstruction; dynamic displacement monitoring; high-speed railway box girder; plate element analysis method

1. Introduction

Up to now, the total operating mileage of high-speed railways in China exceeds 35,000 km, and the total mileage of high-speed railway bridges exceeds 16,000 km. More than 85% of the high-speed railway bridges in China are prestressed concrete simply supported box girders. As is well known, the dynamic displacement is a significant index affecting operation safety and ride comfort of high-speed railway, the important judgment basis to evaluate the vertical stiffness of bridges. And thus dynamic displacement monitoring has become an important and indispensable part of Structural Health Monitoring (SHM) systems. However, the dynamic displacement of high-speed railway box girders is extremely small (the maximum displacement of 32 m standard box girder caused by 300 km/h train is generally less than 1 mm). The dynamic displacement monitoring of high-speed railway box girder, which meets the requirements of intelligent operation and maintenance, has become a critical problem to be solved in the field of Structural Health Monitoring.

In the past decades, worldwide researchers have developed a variety of bridge displacement measurement methods, which could be divided into direct and indirect categories (Lee *et al*. 2006, 2007, Ribeiro *et al*. 2014). For the direct displacement measurement methods, the typical devices are dial indicator, linear variable differential transformers (LVDTs), cable-type displacement sensors, laser, and GPS (Garg *et al*. 2019, Seo 2021a, b, Perry and Guo 2021, Kaloop *et al*. 2017, Zona 2021, Scaioni *et al*. 2018) etc. Due to the limitation of accuracy, installation difficulty, frequency response characteristics, sampling frequency etc., such methods were still difficult to be incorporated in the high-speed railway box girder monitoring, especially for displacement monitoring. For the indirect displacement measurement methods, strain and inclinometer sensors are usually employed for dynamic displacement reconstruction using the strain-displacement or inclination-displacement relationship. Compared to inclinometer sensors, the strain sensors are more mature (Sousa *et al*. 2013, Sun *et al*. 2019), and the measured strain are much more accurate and reliable. Furthermore, strain is sensitive to local structural damage and the identified strain modal parameters were also widely used for damage detection. Therefore, considering the abundant local and global structural information embedded in strain, monitored strain is employed to reconstruct displacement of high-speed railway box girder in this study.

Researchers mainly estimate the structural displacement using the mechanical strain-displacement relationship and the modal transformation algorithm (Esposito and Gherlone 2020, Li and Ulsoy 1999, Kim *et al*. 2011, 2014, Thomas *et*

*Corresponding author, Ph.D., Professor,
E-mail: lishunlong@hit.edu.cn
[a] Ph.D.
[b] Ph.D. Student

ISSN: 1738-1584 (Print), 1738-1991 (Online)

al. 2020, Bernardini *et al*. 2018, Javdani *et al*. 2014). For the displacement curve reconstruction (Jones *et al*. 1998, Kefal *et al*. 2021, Luo *et al*. 2019, Ferreira *et al*. 2017), it is assumed that the curvature of the investigated bridge could be represented by a polynomial function along longitudinal direction. The measured strain was used for the least square curvature curve fitting. Then the displacement curve of the investigated bridge would be obtained by integrating the fitted curvature curve two times. Displacement surface could also be reconstructed using similar surface-patch-fitting method with much more strain sensors (Di 2012, Xu *et al*. 2013). However, the current mechanical strain-displacement relationship is mainly based on the elementary beam deformation theory, which simplifies the investigated bridge into Euler-Bernoulli beams. Such strain-displacement relationship could only be established for the slender beam subjected to pure bending, which satisfies plane section assumption. For typical high-speed railway box girder under two-lane eccentric train load, the bridge produces not only longitudinal bending stress but also constrained torsion warping stress and distortion warping stress. The elementary beam deformation theory-based strain-displacement relationship was no longer valid for such box girders under bend-torsion coupling effects.

The research method of this paper is based on the inverse finite element method (iFEM) to realize the dynamic displacement reconstruction of the high-speed railway box girders. The iFEM (Tessler and Spangler 2004) is a widely used shape-sensing method that reconstructs the displacement field of the structure based on the surface-measured strains. Researchers in related fields have completed various numerical, theoretical and experimental studies on the iFEM algorithm. Gherlone *et al*. (2014) conducted related experimental tests to examine the capabilities of their inverse-frame element. Then, the iFEM methodology was applied in the field of shape sensing of laminated composites and sandwich panels (Cerracchio *et al*. 2015a). Moreover, Kefal *et al*. (2016) introduced a robust four-node quadrilateral inverse-shell element (iQS4) into the field of iFEM research. Subsequently, in order to increase the practical capability of iFEM for composite structures, Kefal *et al*. (2017) newly enhanced Cerracchio's iFEM formulation and developed a novel inverse-shell element, i3-RZT. In addition, the iFEM framework was applied to not only SHM of future aerospace vehicles (Cerracchio *et al*. 2015b, Papa *et al*. 2017, Kefal and Yildiz 2017), but also shape and stress sensing of marine structures (Kefal and Oterkus 2016a, b, Kefal *et al*. 2018). Recently, iFEM is applied to various damage detection strategies for locating cracks/pre-damage regions (Roy *et al*. 2020, Li *et al*. 2020). In addition to the plate/shell structure, a robust iFEM method was introduced for shape sensing of thick/thin beam structures (Savino *et al*. 2019), and related experiments and numerical applications have revealed their high precision and robustness (Liu *et al*. 2018, Song and Liang 2018).

This paper proposes an indirect strain based dynamic displacement reconstruction methodology for high-speed railway box girders. By decoupling the total strain into bending moment induced strain and torque induced strain, the bend induced strain-displacement and the torque induced strain-displacement relationship could be established respectively according to the mechanical properties and the modal transformation algorithm. Thenthe dynamic displacement of the box girder at critical positions could be reconstructed using the superposition of the bending moment and the torque induced displacement. The flow chart of strain based dynamic displacement reconstruction of the box girder is shown in Fig. 1. The paper is organized as follows: section 2 illustrates the theoretical background and procedures of the proposed dynamic displacement reconstruction methodology, including the strain-displacement transformation model establishment, the decoupling of bending moment induced strain and torque induced strain and modal transformation matrix optimization; section 3 presents the numerical simulation and experimental verification of a typical high-speed railway 32 m box girder verifying the accuracy and robustness of the proposed methodology; some conclusions are finally drawn in section 4.

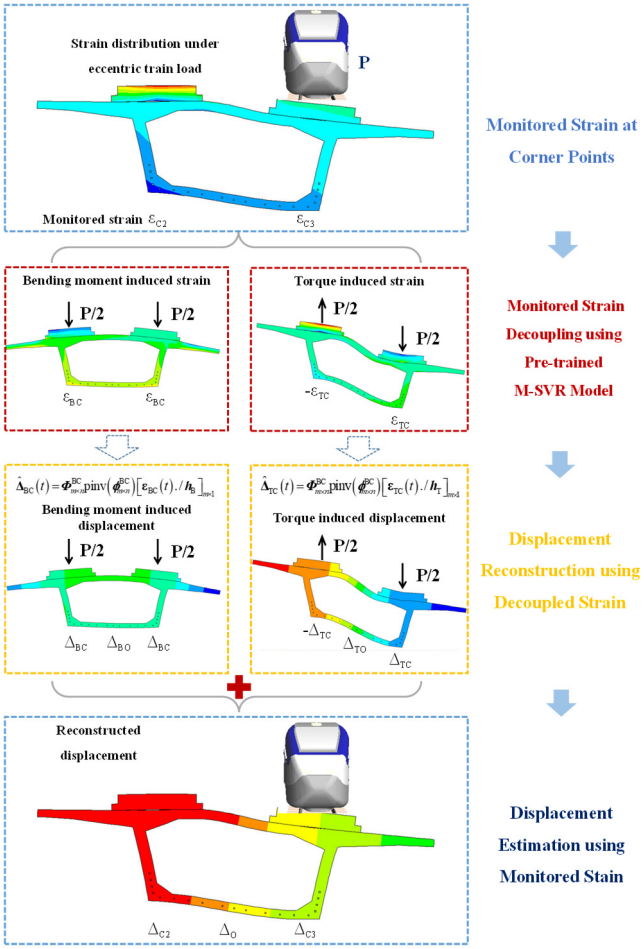

Fig. 1 Flow chart of dynamic displacement reconstruction methodology for high-speed railway box girders

2. Strain based dynamic displacement monitoring

2.1 Strain-displacement reconstruction methodology

Under the eccentric load, the cross section responses can be decomposed into the superposition of the bending moment load and the torque load according to the equivalent load principle on the section of the box girder (Kristek 1979). The torque load can be further decomposed into the superposition of rigid torsional load and distortion load. The aforementioned three kinds of loads would generate longitudinal stress in the cross section of box girders. Therefore, the monitored longitudinal strain ε and vertical displacement Δ at the measured points of the high-speed railway box girder under eccentric load can be expressed as

$$\begin{cases} \varepsilon = \varepsilon_B + \varepsilon_T = \varepsilon_B + \varepsilon_{T,R} + \varepsilon_{T,D} \\ \Delta = \Delta_B + \Delta_T = \Delta_B + \Delta_{T,R} + \Delta_{T,D} \end{cases} \tag{1}$$

where ε_B and Δ_B, ε_T and Δ_T represent the longitudinal strain and vertical displacement caused by bending moment and torque load, respectively. $\varepsilon_{\mathrm{T,R}}and\Delta_{T,R}$, $\varepsilon_{\mathrm{T,D}}$ and $\Delta_{\mathrm{T,D}}$ are the longitudinal strain and vertical displacement under the action of rigid torsional load and distortion load, respectively.

(1) Time-varying bending moment load

The longitudinal bending stress distribution of the bottom plate of box girder with coordinate (x, h_B, z) considering the shear lag effect (Kristek 1979) is shown in Fig. 2 and the corresponding strain $\varepsilon_B(x, h_B, z, t)$ could be expressed as

$$\begin{aligned} &\varepsilon_B(x, h_B, z, t) \\ &= h_B(z)\left[\frac{\partial^2 \Delta_{\mathrm{BC}}(z,t)}{\partial z^2} + \left(1 - \frac{|x|^3}{b^3}\right)\frac{\partial \theta(z,t)}{\partial z}\right] \end{aligned} \tag{2}$$

where $h_B(z)$represents the distance from the centreline of the bottom plate to the centroid of the box girder section and remains time-invariant constant; $\Delta_{\mathrm{BC}}(z,t)$ and $\psi^{\mathrm{BC}}(z,t) = \partial^2 \Delta_{\mathrm{BC}}(z,t)/\partial z^2$ represent the time-varying vertical displacement and curvature of the corner points C2 or C3, as shown in Fig. 2; $\theta(z,t)$ is the maximum difference of the shear rotation angle along the longitudinal bridge section of the investigated box girder.

If the strain sensors were installed at corner points C2 or C3 of the investigated box girder ($x = b$), the time-varying bending moment induced strain would be calculated using Eq. (2) as

$$\varepsilon_{\mathrm{BC}}(z,t) = h_B(z)\phi^{\mathrm{BC}}(z,t) = h_B(z)\partial^2 \Delta_{\mathrm{BC}}(z,t)/\partial z^2 \tag{3}$$

The displacement could be expressed as the product of modal matrix and generalized modal coordinates

$$\Delta_{\mathrm{BC}}(z,t) = \Phi^{\mathrm{BC}}_{1\times n}(z) q^{\mathrm{BC}}_{n\times 1}(t) \tag{4}$$

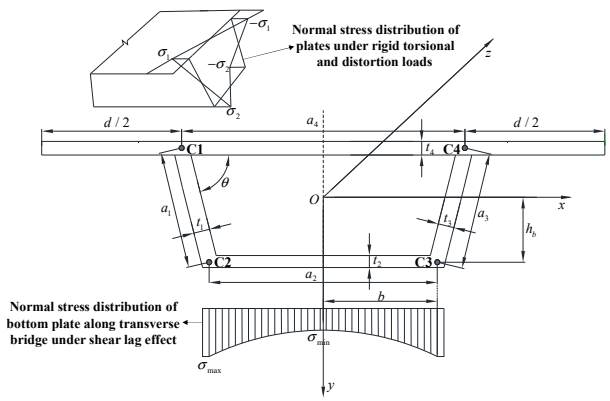

Fig. 2 Schematic diagram of tress distribution of the box girder under bending moment, rigid torsional and distortion load (Xiang 2013)

where $\Phi^{\mathrm{BC}}_{1\times n}(z)$ indicates the vector of the candidate vertical mode shape matrix; and $q^{\mathrm{BC}}_{n\times 1}(t) \in R^{n\times 1}$ is generalized modal coordinates. Then the time-varying bending moment induced strain could be expressed by incorporating Eqs. (3) and (4) as

$$\begin{aligned} \varepsilon_{\mathrm{BC}}(z,t) &= h_B(z)\frac{\partial^2 \Phi^{\mathrm{BC}}_{1\times n}(z)}{\partial z^2} q^{\mathrm{BC}}_{n\times 1}(t) \\ &= h_B(z)\phi^{\mathrm{BC}}_{1\times n}(z) q_{n\times 1}(t) \end{aligned} \tag{5}$$

where $\phi^{\mathrm{BC}}_{1\times n}(z)$ indicates the vector of candidate curvature modal matrix. Supposing that there were *m* strain sensors installed on the corner points along the longitudinal direction of the investigated box girder, then the generalized modal coordinate $\hat{q}_{n\times 1}(t)$ could be estimated as

$$\begin{aligned} &[\boldsymbol{\varepsilon}_{\mathrm{BC}}(t)./h_B]_{m\times 1} = \phi^{\mathrm{BC}}_{m\times n} q^{\mathrm{BC}}_{n\times 1}(t) \\ &\hat{q}^{\mathrm{BC}}_{n\times 1}(t) = \mathrm{pinv}(\phi^{\mathrm{BC}}_{m\times n})[\boldsymbol{\varepsilon}_{\mathrm{BC}}(t)./h_B]_{m\times 1} \end{aligned} \tag{6}$$

where $\mathrm{pinv}(\cdot)$ indicates Penrose-Moore generalized inverse function. Then the dynamic displacement under time-varying bending moment could be reconstructed using the modal matrix and the estimated generalized modal coordinate $\hat{q}^{\mathrm{BC}}_{n\times 1}(t)$

$$\begin{aligned} \widehat{\boldsymbol{\Delta}}_{\mathrm{BC}}(t) &= \Phi^{\mathrm{BC}}_{m\times n}\hat{q}^{\mathrm{BC}}_{n\times 1}(t) \\ &= \Phi^{\mathrm{BC}}_{m\times n}\mathrm{pinv}(\phi^{\mathrm{BC}}_{m\times n})[\boldsymbol{\varepsilon}_{\mathrm{BC}}(t)./h_B]_{m\times 1} \end{aligned} \tag{7}$$

If strain sensors were installed at centre line of the bottom plate of the investigated box girder ($x = 0$), the time-varying bending moment induced strain and displacement would be

$$\begin{aligned} \varepsilon_{\mathrm{BO}}(z,t) &= h_B(z)\left[\frac{\partial^2 \Delta_{\mathrm{BC}}(z,t)}{\partial z^2} + \frac{\partial \theta(z,t)}{\partial z}\right] \\ &= \kappa(z)\varepsilon_{\mathrm{BC}}(z,t) \\ \widehat{\boldsymbol{\Delta}}_{\mathrm{BO}}(t) &= \kappa \cdot \widehat{\boldsymbol{\Delta}}_{\mathrm{BC}}(t) \end{aligned} \tag{8}$$

(2) Time-varying torque load

For rigid torsional load, the cross section of the investigated box girder produces warping normal stress based on the plate element analysis method. The strain-curvature relationship of the corner points (x = b) at the

$$\psi_{\mathrm{T,R}}(z,t) = (1+\beta)\frac{\varepsilon_{\mathrm{T,R}}(z,t)}{a_1 \sin\theta} + \frac{2\varepsilon_{\mathrm{T,R}}(z,t)}{a_2 \tan\theta} = \varepsilon_{\mathrm{T,R}}(z,t)\left(\frac{1+\beta}{a_1 \sin\theta} + \frac{2}{a_2 \tan\theta}\right) = \frac{\varepsilon_{\mathrm{T,R}}(z,t)}{h_T(z)} \quad (9)$$

bottom plate of box girder in Fig. 2 can be expressed as (Xiang 2013) Eq. (9). where $\beta = [a_2^2 t_2 + a_1(a_4 + 2a_2)t_1]/[(a_4+d)^3 t_4/a_4 + a_1 t_1(2a_4 + a_2)]$ and $h_T(z)$ remains time invariant; the definition of geometrical parameter in Eq. (9) is shown in Fig. 2.

Similarly for distortion load, the strain-curvature relation of the corner points at the bottom plate of the box girder can be expressed as (Xiang 2013)

$$\psi_{\mathrm{T,D}}(z,t) = (1+\beta)\frac{\varepsilon_{\mathrm{T,D}}(z,t)}{a_1 \sin\theta} + \frac{2\varepsilon_{\mathrm{T,D}}(z,t)}{a_2 \tan\theta} = \varepsilon_{\mathrm{T,D}}(z,t)\left(\frac{1+\beta}{a_1 \sin\theta} + \frac{2}{a_2 \tan\theta}\right) = \frac{\varepsilon_{\mathrm{T,D}}(z,t)}{h_T(z)} \quad (10)$$

In the same way, the torque induced displacement at the corner points $\widehat{\boldsymbol{\Delta}}_{\mathrm{TC}}(t)$ can also be obtained using the modal transformation method

$$\widehat{\boldsymbol{\Delta}}_{\mathrm{TC}}(t) = \widehat{\boldsymbol{\Delta}}_{\mathrm{T,R}}(t) + \widehat{\boldsymbol{\Delta}}_{\mathrm{T,D}}(t) = \Phi^{\mathrm{BC}}_{m\times n}\mathrm{pinv}(\phi^{\mathrm{BC}}_{m\times n})\{[\boldsymbol{\varepsilon}_{\mathrm{T,R}}(t) + \boldsymbol{\varepsilon}_{\mathrm{T,D}}(t)]./h_T\}_{m\times 1} = \Phi^{\mathrm{BC}}_{m\times n}\mathrm{pinv}(\phi^{\mathrm{BC}}_{m\times n})[\boldsymbol{\varepsilon}_{\mathrm{TC}}(t)./h_T]_{m\times 1} \quad (11)$$

Seen from Eqs. (7) and (11) that although bending moment and torque induced displacement shared the same candidate modal matrix $\Phi^{\mathrm{BC}}_{m\times n}$ and curvature matrix $\phi^{\mathrm{BC}}_{m\times n}$, the selected modal transformation matrix were different from each other taking into account the displacement reconstruction accuracy, which would discussed in Section 2.3.

For the centre line of bottom plate of the investigated box girder (x = 0), the stress distribution of torque load is shown in Fig. 2. The value of the normal stress at the centre line of the bottom plate is zero, and thus the corresponding vertical displacement is zero $\widehat{\boldsymbol{\Delta}}_{\mathrm{TO}}(t) = 0$.

(3) Displacement estimation and parameter determination

It could be seen from Eq. (7) and Eq. (11) that once the monitored strain of the corner points at the bottom plate of the investigated box girder were decoupled into bending moment induced strain $\boldsymbol{\varepsilon}_{\mathrm{BC}}(t)$ and torque induced strain $\boldsymbol{\varepsilon}_{\mathrm{TC}}(t)$, the corresponding displacement $\widehat{\boldsymbol{\Delta}}_{\mathrm{BC}}(t)$ and $\widehat{\boldsymbol{\Delta}}_{\mathrm{TC}}(t)$could be reconstructed using the modal transformation method respectively. Then the vertical displacement of the corner points on the train passing side (as shown in Fig. 1) and the other side would be $\widehat{\boldsymbol{\Delta}}_{\mathrm{C3}}(t) = \widehat{\boldsymbol{\Delta}}_{\mathrm{BC}}(t) + \widehat{\boldsymbol{\Delta}}_{\mathrm{TC}}(t)$ and $\widehat{\boldsymbol{\Delta}}_{\mathrm{C2}}(t) = \widehat{\boldsymbol{\Delta}}_{\mathrm{BC}}(t) - \widehat{\boldsymbol{\Delta}}_{\mathrm{TC}}(t)$ respectively, while the vertical displacement of the centreline could be estimated using Eq. (8) as $\widehat{\boldsymbol{\Delta}}_{O}(t) = \widehat{\boldsymbol{\Delta}}_{\mathrm{BO}}(t) + \widehat{\boldsymbol{\Delta}}_{\mathrm{TO}}(t) = \kappa \cdot \widehat{\boldsymbol{\Delta}}_{\mathrm{BC}}(t)$.

The time-invariant constant parameters $h_B(z)$ and $h_T(z)$ could be estimated by displacement influence line and its curvature curve analysis under the bending moment and torque using Finite Element Model. For the typical 32.0 m high-speed railway box girder in China, the parameter at the mid span would be $h_B(L/2) = 1.541$ and $h_T(L/2) = 0.979$.

2.2 Bending moment and torque induced strain decoupling using M-SVR model

Seen from the section 2.1, decoupling the monitored strain into bending moment and torque induced strain was critical for strain-displacement reconstruction. Obviously, the most effective way for such decoupling would to install strain sensors on both side corners at the bottom plate of the investigated box girder. However, for such a large number of high-speed railway box girders in China, if the dynamic displacement monitoring system is to be built for the entire high-speed railway line, the number of sensors, corresponding data storage system and financial cost etc. would be numerous and unacceptable. Thus, in this study, the strain decoupling would be achieved using monitored strain at one side corner with the help of finite element model analysis, considering reconstruction accuracy and economy using limited sensors.

Supposing that m strain sensors were installed on the one side corner points at the bottom plate of the investigated box girder, the monitored strain time history on the passing side of the train could be demonstrated as $\boldsymbol{\varepsilon}_C \in R^{N\times m}$. The mapping relationship between the monitored strain $\boldsymbol{\varepsilon}_C \in R^{N\times m}$ and the torque induced strain $\boldsymbol{\varepsilon}_{\mathrm{TC}} \in R^{N\times m}$ could be transformed into multi-dimensional estimation problem, and the M-SVR methodology (Sanchez-Fernadez *et al*. 2004) were employed for such mapping

$$\boldsymbol{\varepsilon}_{\mathrm{TC}} = \boldsymbol{\varepsilon}_C \boldsymbol{H} + \boldsymbol{b} + \boldsymbol{\eta} \quad (12)$$

where $\boldsymbol{\eta}$ represents the error matrix, $\boldsymbol{H}$ and $\boldsymbol{b}$ are the weight coefficient matrix and the bias vector respectively. The risk term of the model is added to the loss function of M-SVR to avoid overfitting, so the M-SVR problem can be transformed into

$$\begin{cases} argmin\, L_P(\boldsymbol{H},\boldsymbol{b}) = \dfrac{1}{2}\sum_{k=1}^{m}\|\boldsymbol{H}(:,k)\|^2 + C\sum_{i=1}^{N} L(u_i) \\ u_i = \left\|\boldsymbol{\varepsilon}^i_{\mathrm{TC}} - \boldsymbol{\varepsilon}^i_C\boldsymbol{H} - \boldsymbol{b}\right\| = \sqrt{\left(\boldsymbol{\varepsilon}^i_{\mathrm{TC}} - \boldsymbol{\varepsilon}^i_C\boldsymbol{H} - \boldsymbol{b}\right)\left(\boldsymbol{\varepsilon}^i_{\mathrm{TC}} - \boldsymbol{\varepsilon}^i_C\boldsymbol{H} - \boldsymbol{b}\right)^T} \end{cases} \quad \text{where} \quad L(u_i) = \begin{cases} 0 & u_i < \eta_\kappa \\ (u_i - \eta_\kappa)^2 & u_i > \eta_\kappa \end{cases} \quad (13)$$

where C is the regularization constant and $L(u_i)$ is the

insensitive loss function based on the L_2 norm, η_κ is the upper limit of model error. Given the training datasets from FEM analysis, the M-SVR model parameters can be obtained by iterative weighted least squares (Tuia *et al*. 2011) based on Eq. (13). In this way, the decoupling of the bending moment and the torque induced strain of the corner points at the bottom plate on the passing train side can be achieved using the trained M-SVR model.

The training and testing strain datasets of M-SVR decoupling model could be simulated by UM software, which ensures the reconstruction accuracy while saves a lot of investment.

2.3 Modal transformation matrix optimization

When an eccentrically high-speed train passes over box girders, due to the uniqueness of the spatial distribution of the train load and track direction, limited number of specific mode shapes could be activated to participate in the box girder vibration. Also, seen from Eqs. (7) and (11) that, modal transformation matrix has significant influence on the accuracy of reconstructed displacement. Therefore, it is necessary to optimize the selection of the mode shapes in the modal transformation matrix construction. In this study, the first 20 vertical displacement and 20 curvature mode shapes of the investigated high-speed railway box girder are extracted from the ANSYS model as candidate modal matrixes.

simulated displacement of each concerned section $\Delta_{\mathrm{BC}}(z,t) - \hat{\Delta}_{\mathrm{BC}}(z,t) \in R^{N\times 1}$ were supposed to follow the Gaussian distribution with zero mean. Therefore, the average information entropy Θ (Papadimitriou *et al*. 2000, Karimian and Modarres 2021) of displacement prediction errors could be expressed as

$$\Theta = \sum_{n=1}^{m} \frac{1}{2} ln(2\pi e \hat{\sigma}_n^2) / m \tag{14}$$

where $\hat{\sigma}_n^2$ is the variance estimation of error vector $\Delta_{\mathrm{BC}}(z,t) - \hat{\Delta}_{\mathrm{BC}}(z,t)$. The optimal modal transformation matrix problem can be transformed into minimizing the average information entropy of the predicted displacement error matrix. In recent years, various optimization algorithms have been extensively studied and successfully applied in SHM systems (Nestorovic *et al*. 2015, Barthorpe and Worden 2020, Jalsan *et al*. 2014, Tong *et al*. 2014). Particle Swarm Optimization (Fesharaki and Golabi 2016, Das and Dhang 2020) was employed to solve the optimization problem, while the average information entropy Θ was employed as the fitness function. The smaller the average information entropy of the error matrix, the larger its fitness value. The individual extremum and population extremum positions were updated by comparing the fitness values of the new particles with the individual extremum and the population extremum.

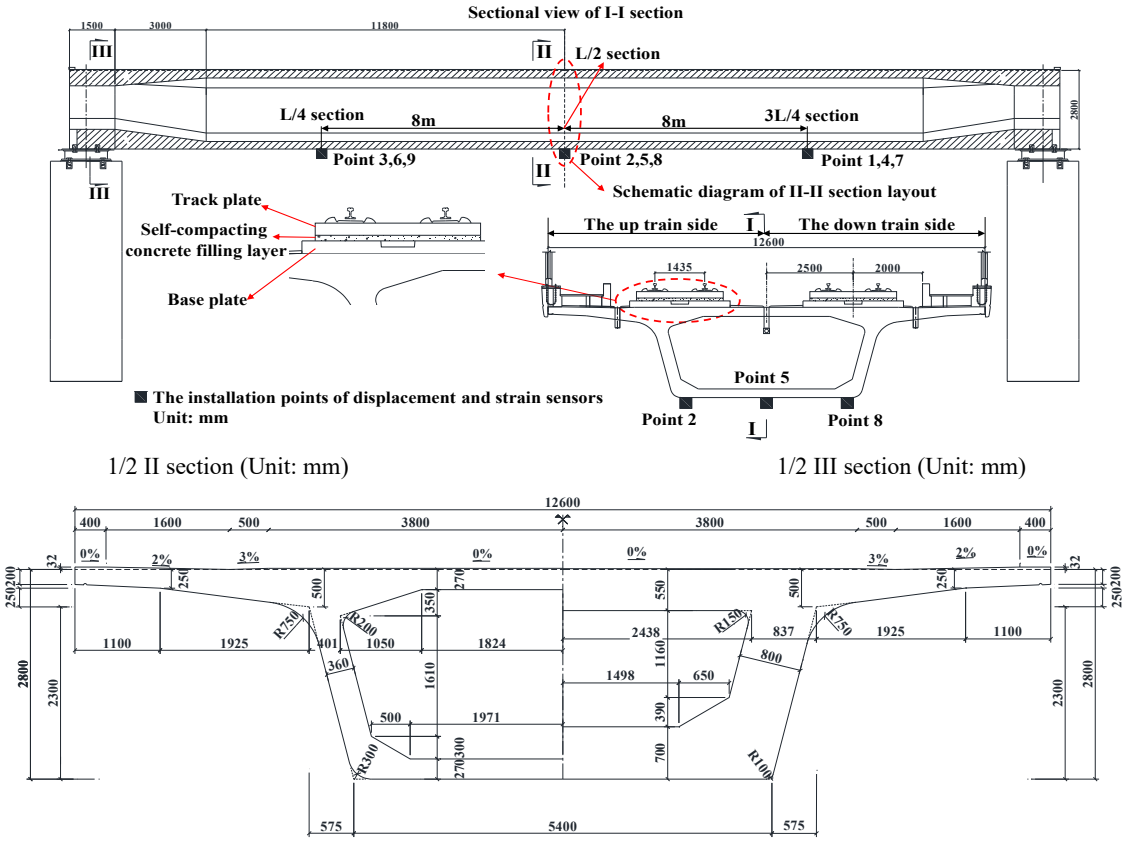

Fig. 3 Design drawings and sensor layout of the investigated 32 m box girder

Assuming that error between reconstructed and

Table 1 Material parameters in the FEM

Item	Element type	Initial/Modified density (kg/m^3)	Initial/Modified Poisson's ratio	Initial elastic modulus (N/m^2)	Modified elastic modulus (N/m^2)
Main girder	Solid65	2549/2681	0.2/ 0.202	3.55×10^{10}	4.29×10^{10}
Self-compacting concrete filling layer, base plate				3.40×10^{10}	3.79×10^{10}
Track plate				3.65×10^{10}	4.06×10^{10}
Other secondary dead loads	Element type	Initial/Modified value (N/m)		Initial elastic modulus(N/m^2)	
	Mass21	$6.845\times10^4/6.702\times10^4$		/	
Prestressed steel	Element type	Density(kg/m^3)	Poisson's ratio	Elastic modulus (N/m^2)	Coefficient of linear expansion
	Link8	8005	0.3	1.95×10^{11}	1.2×10^{-5}

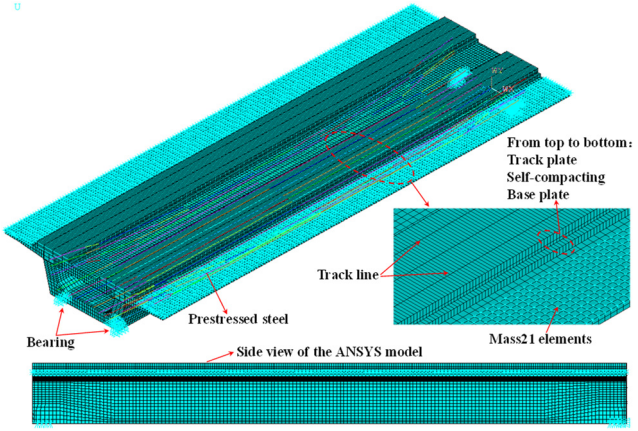

Fig. 4 The various views of the ANSYS model

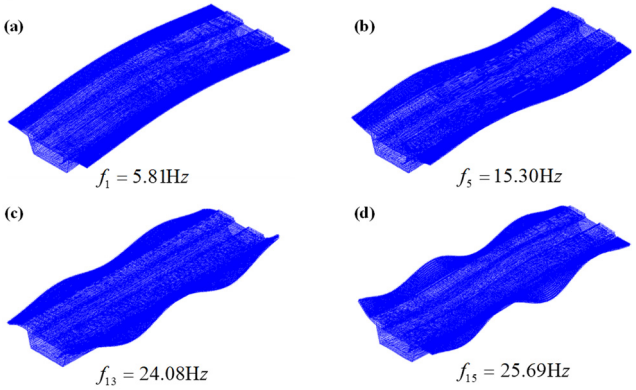

Fig. 5 Several typical mode shapes of the 32 m box girder beam

3. Numerical simulation and experimental verification

3.1 FEM of widely used 32 m high speed railway box girder

According to the design drawings of the widely used high-speed railway box girder as shown in Fig. 3, the three-dimensional (3D) finite element model was established using ANSYS software as shown in Fig. 4. In the FEM, the main girder, track plate, base plate and self-compacting concrete filling layer were modeled by Solid65 elements with a size of 0.2 m, other secondary dead loads such as the protective wall were modeled by Mass21 elements on the bridge deck. There is no modeling of ordinary reinforcements in the FEM, and the influence of ordinary reinforcements is considered by modifying the material parameters of concrete. The prestressed steel was modeled by Link8 elements with a size of 0.1 m, the degrees of freedom of concrete and prestressed steel were coupled in the simulation. For the boundary conditions, the TJQZ spherical bearings at the 2 piers were simulated by fixed hinged supports that are capable of free rotation, unidirectional hinged supports that are capable of free rotation and transversal sliding, unidirectional hinged supports that are capable of free rotation and longitudinal sliding, bidirectional hinged supports that are capable of free rotation, transversal sliding and longitudinal sliding, and their degrees of freedom were coupled in the simulation. In total, the FEM for the investigated bridge consists of 61500 Solid65 elements, 3440 Mass21 elements and 6208 Link8 elements.

The structural parameters of the box girder, such as elastic modulus, density and secondary dead load, were updated according to the dynamic and static properties of the real bridge. The relevant material parameters in the FEM are shown in Table 1. The initial material parameters in Table 1 are obtained according to the design drawings, and the modified material parameters are obtained by updating the FEM according to the first identified frequency of the bridge. The first-order frequency is identified based on the acceleration data collected in the dynamic load test, and the first identified and calculated natural frequency is 5.86 Hz and 5.81 Hz respectively, indicating that the updated finite element model could simulate the dynamic and static performance to a certain extent. Fig. 5. shows several typical mode shapes of the investigated 32 m box girder.

Universal Mechanism (abbreviated UM) is a large general-purpose multi-body system dynamics simulation software from Russia, kinematics and computer modeling and simulation for a variety of two-dimensional and three-dimensional space agencies dynamics calculations, it is widely used in rail transportation, highway transportation,

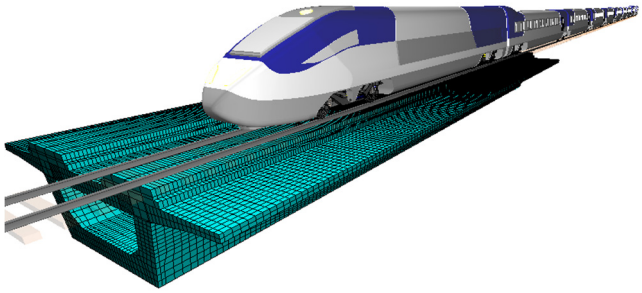

Fig. 6 Schematic diagram of UM multi-body dynamics model

aerospace, construction machinery and robotics and other fields. Multi-body system is a kind of mechanical abstraction of actual mechanism, generally composed of multiple rigid bodies connected by specific hinges and force elements. Several flexible bodies can be introduced to form a rigid-flexible coupling/hybrid system with a multi-rigid body system, such as vehicle-track-bridge dynamic coupling system. Therefore, this study uses UM software to model and simulate the multi-body dynamics of the high-speed railway vehicle-track-bridge system.

Import the ANSYS finite element model into the UM software through the docking interface between ANSYS and UM to form an UM data format. Stiffness constraints are imposed on the bearing area of the investigated bridge in the UM for support simulation. The track was modelled as continuous elastic foundation beam in the UM software. The foundation under the rail was regarded as a parallel and series linear spring damping system connection in the vertical and transverse direction respectively.

The high-speed train was modelled using CRH380, actually operated on the investigated box girder, which consists of 8 carriages and has a capacity of 556 people with standard weight 80kg/person. The train body, bogie and the wheelsets of the CRH380 were modelled as rigid body in accordance with China High-speed Railway Code, which were connected with each other through the primary and secondary suspension system. Finally, adjust the relative positions of the train, bridge, and track according to the actual situation to complete the preparatory work. Fig. 6. shows the schematic diagram of Universal Mechanism (UM) multi-body dynamics model including the investigated 32 m box girder and CRH380 high speed train.

3.2 Decoupling strain using trained M-SVR model

Supposing that CRH380 high speed train passed the investigated box girder at different speeds, the displacement and strain time histories could be obtained at measured points P1~P9, as shown in Fig. 3. According to the theoretical analysis in Section 2.2 and Fig. 2, the measured strain at corner points C2 and C3 (P1, P2, P3 and P7, P8, P9) could be expressed by bending moment and torque induced strain as

$$\begin{cases} \boldsymbol{\varepsilon}_{C2}(t) = \boldsymbol{\varepsilon}_{BC}(t) - \boldsymbol{\varepsilon}_{TC}(t) \\ \boldsymbol{\varepsilon}_{C3}(t) = \boldsymbol{\varepsilon}_{BC}(t) + \boldsymbol{\varepsilon}_{TC}(t) \end{cases} \tag{15}$$

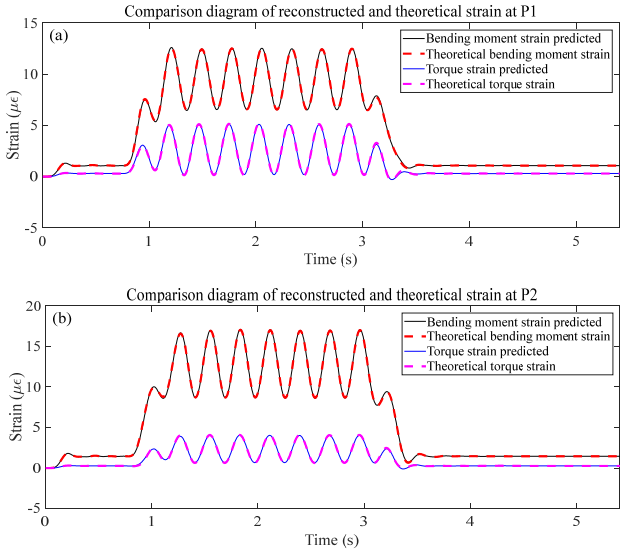

Fig. 7 Comparison diagram of reconstructed and theoretical bending moment and torque strain at 320 km/h speed

Training: The theoretical torque induced strain $\boldsymbol{\varepsilon}_{TC}(t) = [\boldsymbol{\varepsilon}_{C3}(t) - \boldsymbol{\varepsilon}_{C2}(t)]/2$ could be obtained, which were required for training M-SVR model. In this study, the time histories datasets of total strain $\boldsymbol{\varepsilon}_{C3}(t)$ at corner points P1, P2, P3 and the corresponding torque induced strain $\boldsymbol{\varepsilon}_{TC}(t)$ with train speeds 300 km/h, 330 km/h, and 360 km/h would be selected for M-SVR model training considering decoupling accuracy and financial costs. And then, the weight coefficient matrix $\boldsymbol{H}$ and the bias vector $\boldsymbol{b}$ of M-SVR model (as shown in Eq. (12)) could be adjusted using the aforementioned strain time histories. And the relationship between total strain $\boldsymbol{\varepsilon}_{C3}(t)$ and the corresponding torque induced strain $\boldsymbol{\varepsilon}_{TC}(t)$ would be established. Afterwards, the bending moment induced strain and the total strain on the other side corner $\boldsymbol{\varepsilon}_{C2}(t)$ could be calculated by $\boldsymbol{\varepsilon}_{BC}(t) = \boldsymbol{\varepsilon}_{C3}(t) - \boldsymbol{\varepsilon}_{TC}(t)$ and $\boldsymbol{\varepsilon}_{C2}(t) = \boldsymbol{\varepsilon}_{BC}(t) - \boldsymbol{\varepsilon}_{TC}(t)$.

Testing: The time histories of total strain and torque induced strain with train speeds 320 km/h, 350 km/h, and 380 km/h would be chosen as the testing datasets of the trained M-SVR model. Fig. 7 shows the comparison of bending moment and torque induced strain time history between theoretical and predicted by M-SVR model with 320 km/h train speed. It could be seen that the decoupled bending moment and torque induced strain based on the M-SVR model was in good agreement with the theoretical time histories. In addition, it can also be seen that different from the shape curve of the bending moment induced strain, the torque induced strain curve did not have an overall ascending and descending stages. Meanwhile, the torque induced strain occupied an important proportion in the monitored strain, which made the establishment of monitored strain-displacement relationship model directly much more complicated. Therefore, it is necessary and effective to decouple the total strain into bending and torsion induced strain using pre-trained M-SVR model.

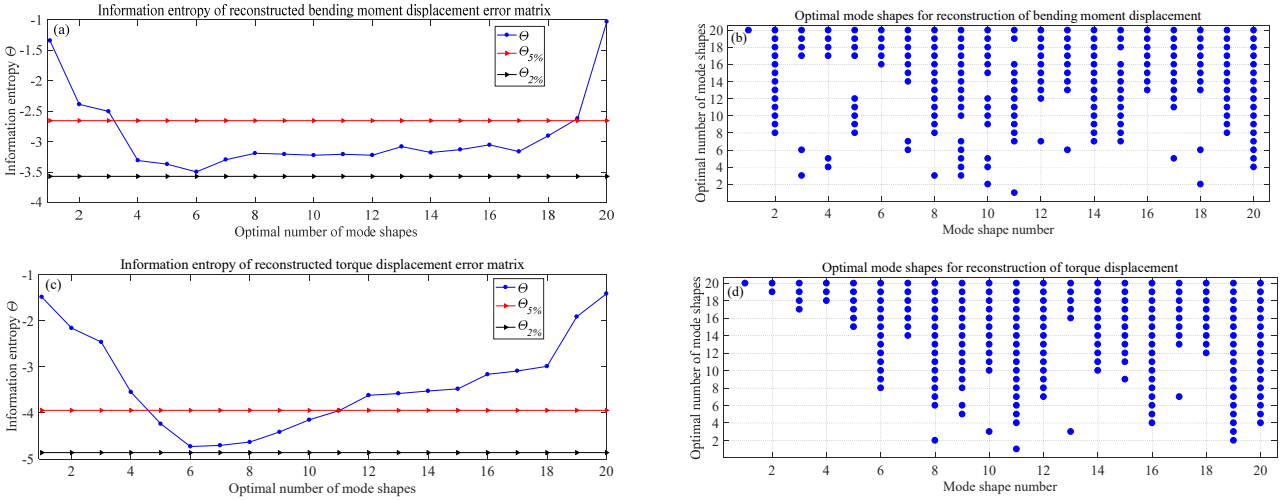

Fig. 8 Information entropy curve and the mode shapes selection with different numbers of optimal mode shapes

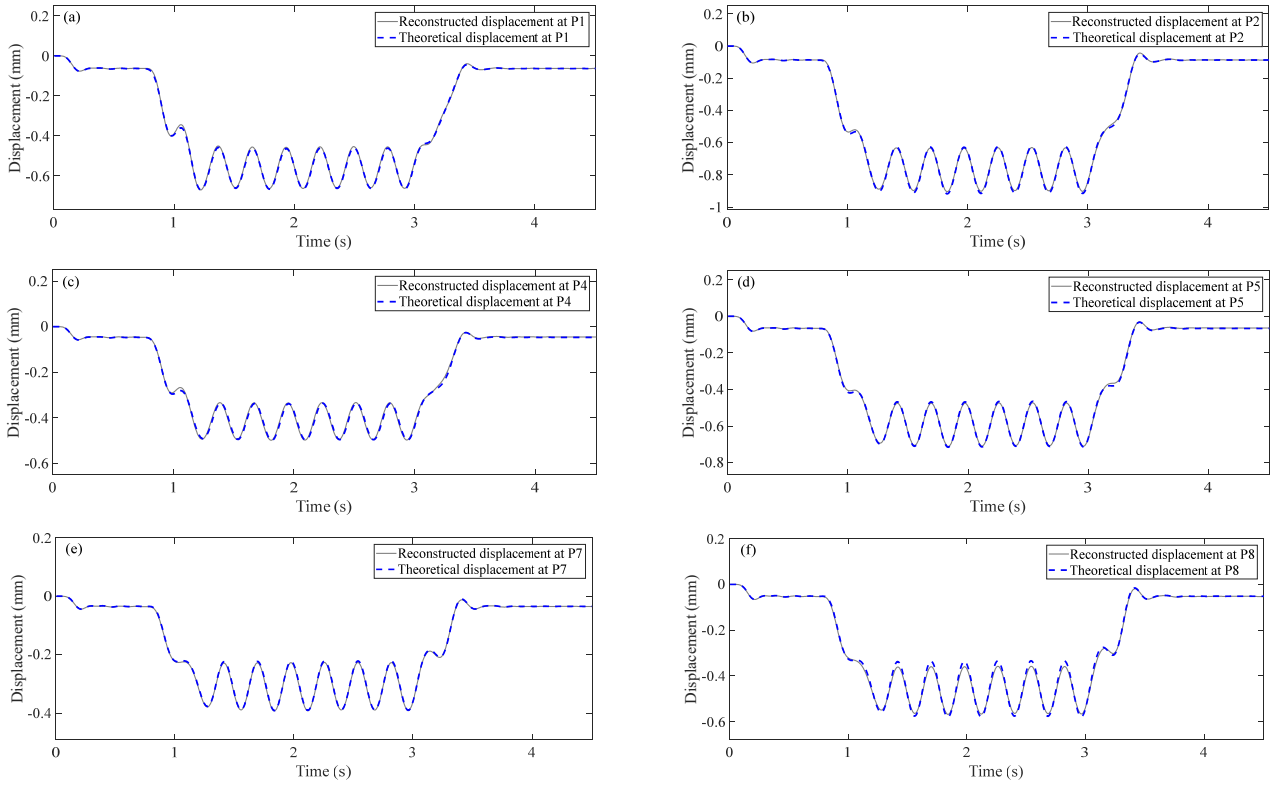

Fig. 9 Comparison of the reconstructed and simulated displacement with 320km/h at different measured points: (a) P1; (b) P2; (c) P4; (d) P5; (e) P7; (f) P8

3.3 Displacement reconstruction using decoupled strain

After the monitored strain decoupling, the corresponding bending moment and torque induce displacement would be reconstructed by modal transforma-tion matrix, optimized by PSO algorithm. Fig. 8 shows the information entropy curve and the mode shapes selection with different numbers of optimal mode shapes. It can be seen from Fig. 8 that for the bending moment and torque induced displacement reconstruction, as the number of selected optimal mode shapes increased, the information entropy of the reconstructed displacement error varied from decline to stability and then to increases. The minimum relative error of displacement reconstruction was less than 5% with the optimal mode shapes. Meanwhile, the number and order of aforementioned optimal mode shapes were different from bending moment to torque induced displacement reconstruction, because the sensitivity of mode shapes to eccentric train load excitation were different.

After the bending moment and torque induced displacement under the eccentric train load were reconstructed, the displacement at measured points P1-P9 could be reconstructed according to Section 2.1. As shown in Fig. 9, the reconstructed displacement time history of the representative measured points was in good agreement with the simulated displacement.

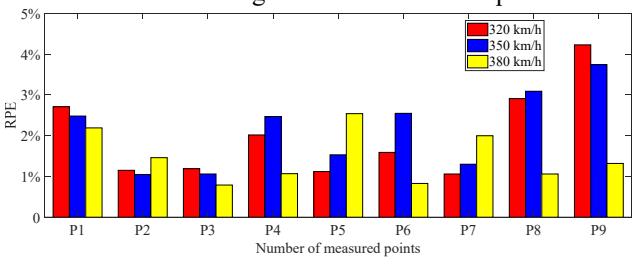

Fig. 10 RPE of reconstructed displacement of each measured point with different velocities

3.4 Dynamic load testing verification

In this study, the relative error percentage (Zhou *et al.* 2019) RPE_i (i = 1, 2…, m) was employed to measure the

Fig. 11 Layout drawing of the dynamic load testing of the investigated typical 32 m box girder

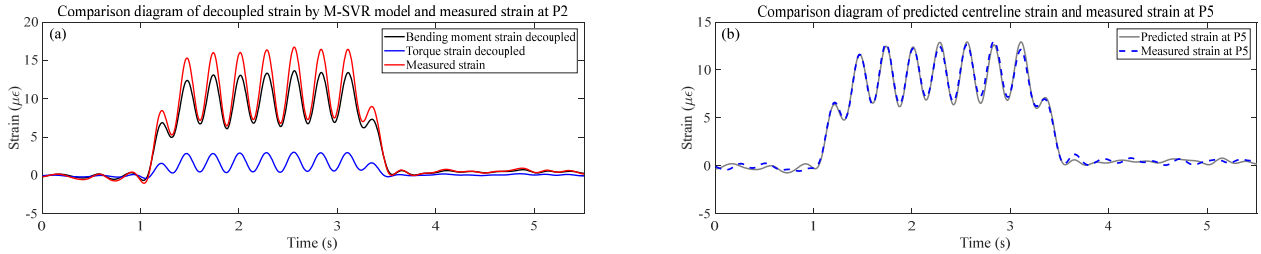

Fig. 12 Comparison diagram of decoupled strain by M-SVR model and predicted centreline strain with measured strain at 328 km/h speed

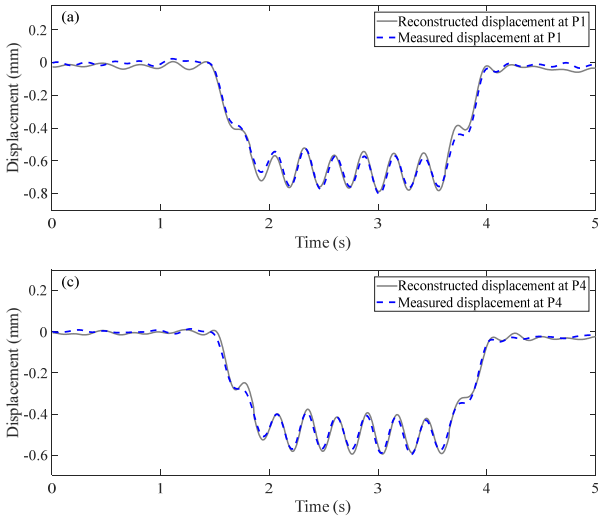

Fig. 13 Comparison of reconstructed and measured displacement duri points: (a) P1; (b) P2; (c) P4; (d) P5

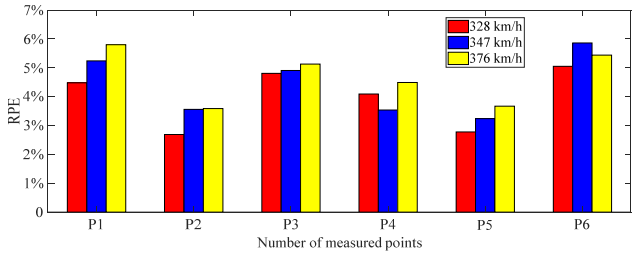

Fig. 14 RPE of reconstructed displacement with different velocities during dynamic load testing

reconstruction accuracy between the reconstructed and the simulated displacement of each measured point.

$$\mathrm{RPE}_i = \left|\Delta - \widehat{\Delta}\right| / |\Delta| \times 100\% \quad (i = 1,2 \cdots m) \qquad (16)$$

Seen from Fig. 10, the relative error percentage for points P1~P9 was within 5% and the maximum was 4.23%, verifying the effectiveness and accuracy of the proposed method in the numerical simulation.

Fig. 11 shows the layout of the dynamic load testing for the investigated typical 32 m box girder, the strain and displacement sensors were installed at points P1, P2, P3, P4, P5, and P6, as shown in Fig. 3. Fig. 11(b) shows a schematic diagram of the installation of various sensors.

Fig. 12 shows the comparison diagram of decoupled strain by M-SVR model and predicted centreline strain with measured strain at 328 km/h speed. Similarly, the torque induced strain occupied an important proportion in the monitored strain, see from Fig. 12(b) that, the predicted centreline strain time history by decoupled bending moment strain using Eq. (8) agreed well with the measured strain at P5. In this study, only strain sensors at points P1, P2 and P3 were employed for strain decoupling and displacement reconstruction.

Fig. 13 shows the comparison between reconstructed and measured displacement during dynamic load testing with 328 km/h, where the strain-displacement reconstruction model was established in Section 3.3. See from Fig. 13 that, the reconstructed displacement time history of the representative measured points agreed well with the measured displacement.

Fig. 14 gives the relative error percentage between the reconstructed and measured displacement for measured points P1~P6. Seen from Fig. 14 that all the relative error percentage fell into 10%, and the maximum was 5.86%. The proposed strain based dynamic displacement monitoring of high-speed railway box girder could be verified for practicability.

4. Conclusions

This paper provides an indirect method for dynamic displacement reconstruction of the high-speed railway box girders considering the coupling effect of bending and torsion. The following conclusions could be drawn:

- Under the coupling effects of bending and torsion, the bending moment and torque induced strain-displacement relationship model should be established separately. The modal transformation matrix has significant impact on the displacement reconstruction accuracy and the sensitivity of mode shapes to bending and torque load were different. The number and order of mode shapes, forming the modal transformation matrix, should be optimized to minimize the displacement reconstruction error.
- Based on the pre-trained M-SVR model by UM simulation datasets, only 3 strain sensors at the corner points of the bottom plate could achieve the decoupling of bending moment and torque induced strain under eccentric train loads. All the relative error percentage fell into 5% and 10% for numerical simulation and the dynamic load testing. The accuracy and effectiveness of the proposed method were verified.

The proposed methodology shed light on the dynamic displacement monitoring of high-speed railway box girders. However, the strain-displacement relationship model was established under the situation that only one train passed through box girder, meeting the displacement transformation requirements in most cases. The strain based displacement reconstruction methodology when two high speed trains passed through the investigated box girder would be studied in the near future.

Acknowledgments

Financial support for this study was provided by NSFC [51922034, 51678204, and 51638007], Heilongjiang Natural Science Foundation for Excellent Young Scholars [YQ2019E025], and China Railway Design Corporation R&D Program [2020YY240603, 2020YY340619].

References

Barthorpe, R.J. and Worden, K. (2020), "Emerging trends in optimal structural health monitoring system design: From sensor placement to system evaluation", *J. Sensor Actuator Networks*, **9**(3). https://doi.org/10.3390/jsan9030031

Bernardini, G., Porcelli, R., Serafini, J. and Masarati, P. (2018), "Rotor blade shape reconstruction from strain measurements", *Aerosp. Sci. Technol.*, **79**, 580-587. https://doi.org/10.1016/j.ast.2018.06.012

Cerracchio, P., Gherlone, M., Di Sciuva, M. and Tessler, A. (2015a), "A novel approach for displacement and stress monitoring of sandwich structures based on the inverse finite element method", *Compos. Struct.*, **127**, 69-76. https://doi.org/10.1016/j.compstruct.2015.02.081.

Cerracchio, P., Gherlone, M. and Tessler, A. (2015b), "Real-time displacement monitoring of a composite stiffened panel subjected to mechanical and thermal loads", *Meccanica*, **50**(10), 2487-2496. https://doi.org/10.1007/s11012-015-0146-8

Das, S. and Dhang, N. (2020), "Structural damage identification of truss structures using self-controlled multi-stage particle swarm optimization", *Smart Struct. Syst., Int. J.*, **25**(3), 345-368. https://doi.org/10.12989/sss.2020.25.3.345

Di, H.T. (2012), "Space curve fitting method based on fiber-optic curvature gages", *Optics Laser Technol*., **44**(1), 290-294. https://doi.org/10.1016/j.optlastec.2011.07.007

Esposito, M. and Gherlone, M. (2020), "Composite wing box deformed-shape reconstruction based on measured strains: Optimization and comparison of existing approaches", *Aerosp. Sci. Technol*., **99**, 105758. https://doi.org/10.1016/j.ast.2020.105758

Ferreira, P., Caetano, E., Ramos, L. and Pinto, P. (2017), "Shape sensing monitoring system based on fiber-optic strain measurements: Laboratory tests", *Experim. Techniq*., **41**(4), 407-420. https://doi.org/10.1007/s40799-017-0187-0

Fesharaki, J.J. and Golabi, S. (2016), "A novel method to specify pattern recognition of actuators for stress reduction based on Particle swarm optimization method", *Smart Struct. Syst*., *Int. J*., **17**(5), 725-742. https://doi.org/10.12989/sss.2016.17.5.725

Garg, P., Moreu, F., Ozdagli, A., Reda Taha, M. and Mascarenas, D. (2019), "Noncontact dynamic displacement measurement of structures using a moving laser Doppler vibrometer", *J. Bridge Eng*., **24**(9), 04019089. https://doi.org/10.1061/(asce)be.1943-5592.0001472.

Gherlone, M., Cerracchio, P., Mattone, M., Di Sciuva, M. and Tessler, A. (2014), "An inverse finite element method for beam shape sensing: theoretical framework and experimental validation", *Smart Mater. Struct*., **23**(4), 045027. https://doi.org/10.1088/0964-1726/23/4/045027

Jalsan, K.E., Soman, R.N., Flouri, K., Kyriakides, M.A., Feltrin, G. and Onoufriou, T. (2014), "Layout optimization of wireless sensor networks for structural health monitoring", *Smart Struct. Syst*., *Int. J*., **14**(1), 39-54. https://doi.org/10.12989/sss.2014.14.1.039

Javdani, S., Fabian, M., Ams, M., Carlton, J., Sun, T. and Grattan, K.T.V. (2014), "Fiber Bragg grating-based system for 2-D analysis of vibrational modes of a steel propeller blade", *J. Lightwave Technol*., **32**(23), 3991-3997. https://doi.org/10.1109/jlt.2014.2361631

Jones, R.T., Bellemore, D.G., Berkoff, T.A., Sirkis, J.S., Davis, M.A., Putnam, M.A., Friebele, E.J. and Kersey, A.D. (1998), "Determination of cantilever plate shapes using wavelength division multiplexed fiber Bragg grating sensors and a least-squares strain-fitting algorithm", *Smart Mater. Struct*., **7**(2), 178-188. https://doi.org/10.1088/0964-1726/7/2/005

Kaloop, M.R., Elbeltagi, E., Hu, J.W. and Elrefai, A. (2017), "Recent advances of structures monitoring and evaluation using GPS-time series monitoring systems: A review", *ISPRS Int. J. Geo-Info*., **6**(12), 382. https://doi.org/10.3390/ijgi6120382

Karimian, S.F. and Modarres, M. (2021), "Acoustic emission signal clustering in CFRP laminates using a new feature set based on waveform analysis and information entropy analysis", *Compos. Struct*., **268**, 113987. https://doi.org/10.1016/j.compstruct.2021.113987

Kefal, A. and Oterkus, E. (2016a), "Displacement and stress monitoring of a chemical tanker based on inverse finite element method", *Ocean Eng*., **112**, 33-46. https://doi.org/10.1016/j.oceaneng.2015.11.032

Kefal, A. and Oterkus, E. (2016b), "Displacement and stress monitoring of a Panamax containership using inverse finite element method", *Ocean Eng*., **119**, 16-29. https:// doi.org/10.1016/j.oceaneng.2016.04.025

Kefal, A. and Yildiz, M. (2017), "Modeling of sensor placement strategy for shape sensing and structural health monitoring of a wing-shaped sandwich panel using inverse finite element method", *Sensors*, **17**(12), 2775. https://doi.org/10.3390/s1712775

Kefal, A., Oterkus, E., Tessler, A. and Spangler, J.L. (2016), "A quadrilateral inverse-shell element with drilling degrees of freedom for shape sensing and structural health monitoring", *Eng. Sci. Technol.-Int. J.-Jestech*, **19**(3), 1299-1313. https://doi.org/10.1016/j.jestch.2016.03.006

Kefal, A., Tessler, A. and Oterkus, E. (2017), "An enhanced inverse finite element method for displacement and stress monitoring of multilayered composite and sandwich structures", *Compos. Struct*., **179**, 514-540. https://doi.org/10.1016/j.compstruct.2017.07.078

Kefal, A., Mayang, J.B., Oterkus, E. and Yildiz, M. (2018), "Three dimensional shape and stress monitoring of bulk carriers based on iFEM methodology", *Ocean Eng*., **147**, 256-267. https://doi.org/10.1016/j.oceaneng.2017.10.040

Kefal, A., Tabrizi, I.E., Yildiz, M. and Tessler, A. (2021), "A smoothed iFEM approach for efficient shape-sensing applications: Numerical and experimental validation on composite structures", *Mech. Syst. Signal Process*., **152**, 107486. https://doi.org/10.1016/j.ymssp.2020.107486

Kim, H.I., Kang, L.H. and Han, J.H. (2011), "Shape estimation with distributed fiber Bragg grating sensors for rotating structures", *Smart Mater. Struct*., **20**(3), 035011. https://doi.org/10.1088/0964-1726/20/3/035011

Kim, H.-I., Han, J.-H. and Bang, H.-J. (2014), "Real-time deformed shape estimation of a wind turbine blade using distributed fiber Bragg grating sensors", *Wind Energy*, **17**(9), 1455-1467. https://doi.org/10.1002/we.1644

Kristek, V. (1979), *Theory of Box Girders*, John Wiley and Sons, New York, NY, USA.

Lee, J.J., Cho, S., Tae, L.W., Shinozuka, M., Yun, C.B. and Lee, C.-G. (2006), "Evaluation of bridge load carrying capacity based on dynamic displacement measurement using real-time image processing techniques", *Steel Struct*., **6**(5), 377-385.

Lee, J.J., Fukuda, Y., Shinozuka, M., Cho, S. and Yun, C.B. (2007), "Development and application of a vision-based displacement measurement system for structural health monitoring of civil structures", *Smart Struct. Syst*., *Int. J*., **3**(3), 373-384. https://doi.org/10.12989/sss.2007.3.3.373

Li, C.J. and Ulsoy, A.G. (1999), "High-precision measurement of tool-tip displacement using strain gauges in precision flexible line boring", *Mech. Syst. Signal Process*., **13**(4), 531-546. https://doi.org/10.1006/mssp.1999.1223

Li, M., Kefal, A., Cerik, B.C. and Oterkus, E. (2020), "Dent damage identification in stiffened cylindrical structures using inverse Finite Element Method", *Ocean Eng*., **198**, 106944. https://doi.org/10.1016/j.oceaneng.2020.106944

Liu, M., Zhang, X., Song, H., Wang, J. and Zhou, S. (2018), "Reconstruction algorithm for obtaining the bending deformation of the base of heavy-duty machine tool using inverse Finite Element Method", *Metrol. Measur. Syst*., **25**(4), 727-741. https://doi.org/10.24425/mms.2018.124878

Luo, Z., Li, J., Hong, G. and Li, H. (2019), "Strain-based displacement field reconstruction method for thin rectangular plate through orthogonal deflection curves bridging", *Struct. Control Health Monitor*., **27**(1), e2457. https://doi.org/10.1002/stc.2457

Nestorovic, T., Trajkov, M. and Garmabi, S. (2015), "Optimal placement of piezoelectric actuators and sensors on a smart beam and a smart plate using multi-objective genetic algorithm", *Smart Struct. Syst*., *Int. J*., **15**(4), 1041-1062. https://doi.org/10.12989/sss.2015.15.4.1041

Papa, U., Russo, S., Lamboglia, A., Del Core, G. and Iannuzzo, G. (2017), "Health structure monitoring for the design of an innovative UAS fixed wing through inverse finite element method (iFEM)", *Aerosp. Sci. Technol*., **69**, 439-448. https://doi.org/10.1016/j.ast.2017.07.005

Papadimitriou, C., Beck, J.L. and Au, S.K. (2000), "Entropy-based optimal sensor location for structural model updating", *J. Vib. Control*, **6**(5), 781-800. https://doi.org/10.1177/107754630000600508

Perry, B.J. and Guo, Y. (2021), "A portable three-component displacement measurement technique using an unmanned aerial vehicle (UAV) and computer vision: A proof of concept", *Measurement*, **176**, 109222. https://doi.org/10.1016/j.measurement.2021.109222

Ribeiro, D., Calcada, R., Ferreira, J. and Martins, T. (2014), "Non-contact measurement of the dynamic displacement of railway bridges using an advanced video-based system", *Eng. Struct.*, **75**, 164-180. https://doi.org/10.1016/j.engstruct.2014. 04.051

Roy, R., Gherlone, M. and Surace, C. (2020), "Damage localisation in thin plates using the inverse finite element method", *Proceedings of the 13th International Conference on Damage Assessment of Structures*, Porto, Portugal, July.

Sanchez-Fernadez, M., de-Prado-Cumplido, M., Arenas-Garcia, J. and Perez-Cruz, F. (2004), "SVM multiregression for nonlinear channel estimation in multiple-input multiple-output systems", *IEEE Transact. Signal Process.*, **52**(8), 2298-2307. https://doi.org/10.1109/tsp.2004.831028

Savino, P., Gherlone, M. and Tondolo, F. (2019), "Shape sensing with inverse finite element method for slender structures", *Struct. Eng. Mech., Int. J.*, **72**(2), 217-227. https://doi.org/10.12989/sem.2019.72.2.217

Scaioni, M., Marsella, M., Crosetto, M., Tornatore, V. and Wang, J. (2018), "Geodetic and remote-sensing sensors for dam deformation monitoring", *Sensors*, **18**(11), 3682. https://doi.org/10.3390/s18113682

Seo, H. (2021a), "Tilt mapping for zigzag-shaped concrete panel in retaining structure using terrestrial laser scanning", *J. Civil Struct. Health Monitor*. https://doi.org/10.1007/s13349-021-00484-x

Seo, H. (2021b), "Long-term Monitoring of zigzag-shaped concrete panel in retaining structure using laser scanning and analysis of influencing factors", *Optics Lasers Eng.*, **139**, 106498. https://doi.org/10.1016/j.optlaseng.2020.106498.

Song, X. and Liang, D. (2018), "Dynamic displaceMent prediction of beam structures using fiber bragg grating sensors", *Optik*, **158**, 1410-1416. https://doi.org/10.1016/j.ijleo.2018.01.013

Sousa, H., Cavadas, F., Henriques, A., Bento, J. and Figueiras, J. (2013), "Bridge deflection evaluation using strain and rotation measurements", *Smart Struct. Syst., Int. J.*, **11**(4), 365-386. https://doi.org/10.12989/sss.2013.11.4.365

Sun, L.M., Zhang, W. and Nagarajaiah, S. (2019), "Bridge real-time damage identification method using inclination and strain measurements in the presence of temperature variation", *J. Bridge Eng.*, **24**(2), 04018111. https://doi.org/10.1061/(ASCE)BE.1943-5592.0001325

Tessler, A. and Spangler, J.L. (2004), "Inverse FEM for full-field reconstruction of elastic deformations in shear deformable plates and shells", *Proceedings of the 2nd European Workshop on Structural Health Monitoring*, Munich, Germany, January.

Thomas, J., Gurusamy, S., Rajanna, T.R. and Asokan, S. (2020), "Structural shape estimation by mode shapes using fiber Bragg grating sensors: A genetic algorithm approach", *IEEE Sensors J.*, **20**(6), 2945-2952. https://doi.org/10.1109/Jsen.2019.2934366

Tong, K.H., Bakhary, N., Kueh, A.B.H. and Yassin, A.Y.M. (2014), "Optimal sensor placement for mode shapes using improved simulated annealing", *Smart Struct. Syst., Int. J.*, **13**(3), 389-406. https://doi.org/10.12989/sss.2014.13.3.389

Tuia, D., Verrelst, J., Alonso, L., Perez-Cruz, F. and Camps-Valls, G. (2011), "Multioutput Support Vector Regression for Remote Sensing Biophysical Parameter Estimation", *IEEE Geosci. Remote Sens. Lett.*, **8**(4), 804-808. https://doi.org/10.1109/lgrs.2011.2109934

Xiang, H. (2013), *Higher Bridge Design Theory*, China Communications Press, Beijing, China. [In Chinese]

Xu, J., Zhang, H., Zhu, X., Li, L. and Ding, P. (2013), "Curve surface fitting based on an improved genetic algorithm", *Proceedings of 2013 6th International Congress on Image and Signal Processing*, Hangzhou, China, December.

Zhou, J.Z., Cai, Z., Kang, L., Tang, B.F. and Xu, W.H. (2019), "Deformation sensing and electrical compensation of smart skin antenna structure with optimal fiber Bragg grating strain sensor placements", *Compos. Struct.*, **211**, 418-432. https://doi.org/10.1016/j.compstruct.2018.12.048

Zona, A. (2021), "Vision-based vibration monitoring of structures and infrastructures: An overview of recent applications", *Infrastruct.*, **6**(1), 4. https://doi.org/10.3390/infrastructures6010004

CC